

Hardware-Accelerated Geometrical Simulation of Biological and Engineered In-Air Ultrasonic Systems

Wouter Jansen, and Jan Steckel

Cosys-Lab, University of Antwerp, 2000 Antwerp, Belgium
Flanders Make Strategic Research Centre, 3920 Lommel, Belgium

Abstract—The deployment of in-air acoustic sensors for industrial monitoring and autonomous robotics has grown significantly, often drawing inspiration from biological echolocation. However, developing and validating these systems in existing simulation frameworks remains challenging due to the computational cost of simulating high-frequency wave propagation in large, dynamic, and complex environments. While wave-based methods offer high accuracy, they scale poorly with frequency and volume. Conversely, existing geometric acoustic solvers often lack support for dynamic scenes, complex diffraction, or closed-loop robotic integration. In this work, we introduce SonoTraceUE, a high-fidelity acoustic simulation framework built as a plugin for Unreal Engine. By using a hardware-accelerated ray tracing-based specular reflection model, and a curvature-based Monte Carlo diffraction model, the system enables near real-time simulation of active and passive acoustic sensing in dynamic, multi-material environments. We validate the framework through two distinct experimental domains: a bioacoustic study and a robotics experiment. Our results demonstrate that SonoTraceUE achieves high correlation with real-world spectral and spatial data. The framework provides a versatile platform for synthetic data generation, hypothesis testing in bioacoustics, and the rapid prototyping of closed-loop robotic systems that use acoustic sensing.

Index Terms—Simulation, sonar, microphone arrays, sound source localization, acoustic signal processing, ultrasound

I. INTRODUCTION

The deployment of in-air acoustic sensors has accelerated over the last decade in a variety of industrial and research sectors, driven by their unique sensing capability and versatility in environments where other modalities may fail. On the one hand, these systems are passively used to monitor other acoustic energy sources. Examples include non-contact fault detection in machinery [1], [2], [3], [4], [5], and the identification of pressurized gas or air leaks in industrial infrastructure [6], [7], [8]. On the other hand, active acoustic systems, specifically pulse-echo sensors, have seen increased adoption as sensing components in robotics applications.

For autonomous navigation and mapping, active acoustics provide a robust alternative to optical systems such as LiDAR and cameras, particularly in scenarios where visual occlusion caused by dust, fog, smoke, or darkness renders optical data unreliable [9], [10], [11].

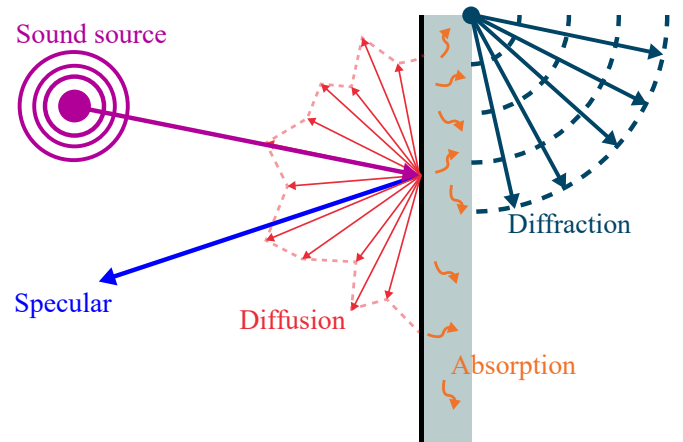


Fig. 1. The various acoustic phenomena that are modeled in the abstraction model as proposed in this paper. The big omissions are refraction and more complex forms of medium transmission (e.g., for in-water simulation). Specular, diffuse, and absorption are simulated directly using ray tracing. In contrast, diffraction uses a Monte Carlo approximation to the wave equation solution, based on the local curvature calculated from the scene geometry.

The development of these engineered systems frequently draws inspiration from biology. Nature offers highly sophisticated in-air acoustic models, most notably in bat species that rely on echolocation to navigate complex environments and capture prey [12], [13], [14].

Whether investigating these biological mechanisms or engineering their artificial counterparts, simulation and modeling can be an indispensable stage when working with these systems. It allows researchers to model specific sensor configurations [15], [16], test scenarios where data is not (yet) available [17], [18], generate large synthetic datasets [19], and validate applications in safe and controlled environments before real-world deployment [20], [21]. Specifically for biological systems, simulation and modeling allow insight into how some species use sound as input and into how they behave. They can also help take the design and application of bio-inspired human-made sensors to the next level [22], [23], [24].

However, simulating acoustic propagation remains computationally challenging, and the choice of technique depends strongly on the problem’s scale and frequency. Sound propagation can be divided into several sub-models, including specular

and diffuse reflections, absorption, refraction, and diffraction. These are visualized in Figure 1. Depending on the desired abstraction model, simulation can only tackle some of these phenomena. Wave-based methods, such as the Finite Element Method (FEM) and the Boundary Element Method (BEM), solve the Helmholtz equation directly to describe wave propagation in the frequency domain. These methods provide exact solutions for the amplitude and phase of the sound pressure at every point in a domain, making them ideal for near-field simulation and detailed analysis of bounded problems. However, this accuracy comes at the cost of computation; as the frequency increases, the required mesh density (geometric resolution) grows drastically. The computational time required to solve the sparse matrices generated by FEM is typically $\mathcal{O}(N^2)$, depending on the solver. And as BEM produces a dense matrix, it typically requires $\mathcal{O}(N^3)$ operations using standard direct solvers. Consequently, FEM and BEM are often limited to small geometrical scales or low frequencies.

To address scenarios involving larger environments and higher frequencies (ultrasound), as typically seen in echolocation scenarios, geometric acoustics (or ray acoustics) offers a different abstraction model. Unlike the full-wave equation, ray acoustics models sound propagation as rays along which acoustic energy is transported, a technique similar to those used in the optical spectrum. This approach is valid when objects are acoustically large but can be ill-suited when, for example, diffraction effects are required, as they are generally not ideally modeled with geometric acoustics [25]. In general, ray acoustics allows the simulation of complex, large-scale geometries with mid-to-high-frequency detail that would be impossible or impractical to resolve using wave-based methods. However, the physical dimensions of the scene should be significantly greater than the signal wavelength so that the objects of interest in that scene have high Helmholtz numbers.

In our previous work, we introduced SonoTraceLab[26], an open-source MATLAB simulation framework that uses a ray-based acoustic model. It was purpose-built to fill a gap left by commercial and existing open-source solutions, specifically for 3D ensonification studies, synthetic data generation, and closed-loop testing of biological hypotheses within the frequency range of 20 kHz to 200 kHz. SonoTraceLab demonstrated effectiveness in providing insights into biological echolocation while reducing the complexity of physical experiments.

Nevertheless, it faced some architectural limitations. The environment relied on static 3D meshes with a single globally defined surface material, modeled using the Bidirectional Reflectance Distribution Function (BRDF). These limitations restricted the ability to model complex, dynamic, multi-material scenes. Furthermore, while the core ray tracing was GPU-accelerated, reliance on MATLAB introduced latency, limiting performance. It also lacked support for multiple simultaneous acoustic sources and was not optimized for rapid scenario creation, as it lacked a 3D editor interface.

In this paper, we introduce SonoTraceUE, a novel implementation that overcomes these scalability and usability constraints



Fig. 2. An example of a large forest environment simulated with SonoTraceUE in Unreal Engine, consisting of 96 unique 3D meshes totaling over 10 000 instances for a combined 21 000 000 triangles. The colored points shown in the image are representative of a small portion of the simulated points by the simulation of a bat, which has two receivers and one emitter in this scenario. A video of the simulation running in this scene is available as supplementary material and online [28].

and that is built upon the Unreal Engine framework [27]. As a multi-platform real-time 3D rendering engine, Unreal offers high-fidelity visualization and optical rendering, along with a versatile editor for creating and scripting dynamic scenarios across large environments. SonoTraceUE leverages this architecture as a plugin, enabling a user-friendly workflow for simulating acoustic systems in large-scale, high-fidelity, and dynamic scenes, as shown in the example in Figure 2. By leveraging hardware-accelerated ray tracing, the framework achieves near-real-time simulation of multiple active or passive acoustic systems interacting with fully modeled BRDF surface properties.

We situate our work within the state of the art in acoustic system simulation and detail the methodological advancements of SonoTraceUE over its predecessor. We present a series of robotic experiments comparing simulated and real-world acoustic odometry and localization to validate the framework’s fidelity. Beyond validation, we demonstrate its capabilities in scenarios that are impractical to replicate physically, thereby deepening our understanding of biological echolocation. We analyze the computational trade-offs of geometric simulation at various resolutions and conclude with our vision for the future trajectory of geometric acoustic simulation.

II. RELATED WORKS

The landscape of acoustic simulation is vast, with methodologies and simulation frameworks often purpose-built for specific frequency ranges, domains, mediums, or applications. As acoustic wave propagation is well understood [25], the level of abstraction required determines which simulation model fits best. Broadly, these can be categorized into wave-based numerical methods, geometric acoustics, and domain-specific solvers for biomedical or robotic applications.

A. WAVE-BASED SIMULATION

Wave-based and multiphysics solvers are often used for high-fidelity analysis of wave phenomena, such as diffraction, interference, and resonance in complex media. FEM[29], [30] and BEM[31] are the industry standard approaches. Several commercial multiphysics platforms offer robust solvers such as COMSOL [32], ANSYS[33], and Siemens SimCenter 3D [34]. These tools excel in analyzing bounded problems, for example, for automotive cabin acoustic analysis or component vibration. Similarly, k-Wave, an open-source MATLAB framework, uses a k-space pseudo-spectral method to simulate wave propagation [35]. Field II is also a widely cited reference for simulating the spatial impulse response of linear ultrasonic transducers [36]. These wave-based approaches have a high computational cost but do offer high simulation accuracy. As the simulation frequency increases to the ultrasonic range, the required mesh density becomes prohibitively expensive for large-scale, three-dimensional environments, rendering them less suitable for simulating extensive robotic navigation tasks. Methods based on FEM generally scale cubically with voxel size in 3D, which can become computationally problematic for large dynamic scenes [37].

B. GEOMETRIC ACOUSTICS

To address the computational scaling issues of wave-based methods, geometric acoustics approximates sound propagation in a different way. Within this domain, two primary techniques exist: the Image-Source Method (ISM) and ray tracing. ISM geometrically mirrors the sound source across reflective boundaries to calculate the exact path of specular reflections [38]. While highly accurate for early reflections, its computational cost grows exponentially with the order of reflections. Ray tracing employs a sampling approach, casting discrete rays into the environment to estimate acoustic energy propagation [39], [40], [41]. This stochastic approach makes ray tracing significantly more efficient for modeling complex geometries and late reverberation. Commercial packages such as Odeon [42] and EASE [43] combine image-source methods with ray tracing to predict parameters like reverberation time and speech intelligibility. The previously mentioned Siemens SimCenter 3D also includes a geometric acoustic option [44]. Research-oriented tools also exist, such as RAVEN, developed by Schröder et al., which offers real-time binaural auralization [18]. The MATLAB Audio Toolbox also includes a stochastic ray tracer for room impulse response generation [45]. Additionally, the web-based CRAM tool has provided an educational platform for understanding these phenomena[46]. While these systems are highly validated for audible frequencies in static environments, they often lack support for the larger dynamic scene changes required in robotics without computationally expensive pre-calculation phases. Furthermore, integrating these standalone applications into a closed-loop robotic control stack can be challenging.

Geometric acoustics shares a fundamental mathematical lineage with optical ray tracing to improve computational efficiency [47]. Modern optical rendering relies on path tracing,

which solves the rendering equation by stochastically tracing millions of light paths. Recently, researchers have begun adapting these mature optical frameworks for acoustics. For instance, Cao et al. adapted bidirectional path tracing to solve the acoustic rendering equation [48]. At the same time, Schissler et al. leveraged the NVIDIA OptiX graphics framework to achieve real-time simulation of high-order diffraction [49]. Finally, Finnendahl et al. used the differentiable rendering engine Mitsuba 3 to implement differentiable acoustic path tracing [50], allowing the simulation of inverse problems such as recovering scene parameters from observations.

C. ROBOTICS SIMULATION

In the field of robotics, high-fidelity visual and physical simulation is well established through platforms such as Gazebo [51], NVIDIA Isaac Sim [52], and CARLA [53]. These simulators excel at rigid-body dynamics, photorealistic rendering, and the simulation of optical sensors such as LiDAR and cameras.

However, their acoustic simulation capabilities are often limited. Acoustic sensors are typically modeled as idealized ray casts or simple object-collision interaction calculations, lacking the complex multi-path propagation, diffraction, and frequency-dependent absorption required for realistic sonar or acoustic scene analysis. Cosys-AirSim, which, like our proposed solution, leverages Unreal Engine to introduce more advanced sensor models, includes a CPU-based geometric wave simulation implementation for active and passive sensors such as radar and sonar[54], [55], but lacks complex per-surface BRDF modeling, support for dynamic scenes for passive sensing, and arbitrary multi-receiver/multi-emitter array configurations.

D. SONOTRACELAB

Our previous open-source framework, SonoTraceLab[26], aimed to bridge the gap between biological studies and engineering simulation by using a MATLAB-based ray-acoustic solver. It provided a tool for 3D ensonification experiments and synthetic data generation for medium-sized static scenes. It supported defining surface material properties using a BRDF. It used a GPU-accelerated ray tracing implementation running on NVIDIA CUDA for fast calculation of the specular reflections. It could simulate a single sound source and multiple receivers. However, reliance on the MATLAB interpretation layer prevented true high performance in larger environments, and the system was constrained to static meshes with a single definition of material properties. Using MATLAB also does not offer a user-friendly interface for scenario creation. Our proposed approach follows and implements the same validated and demonstrated simulation technique as in SonoTraceLab, with additional improvements and features, as well as changes to the technical implementation.

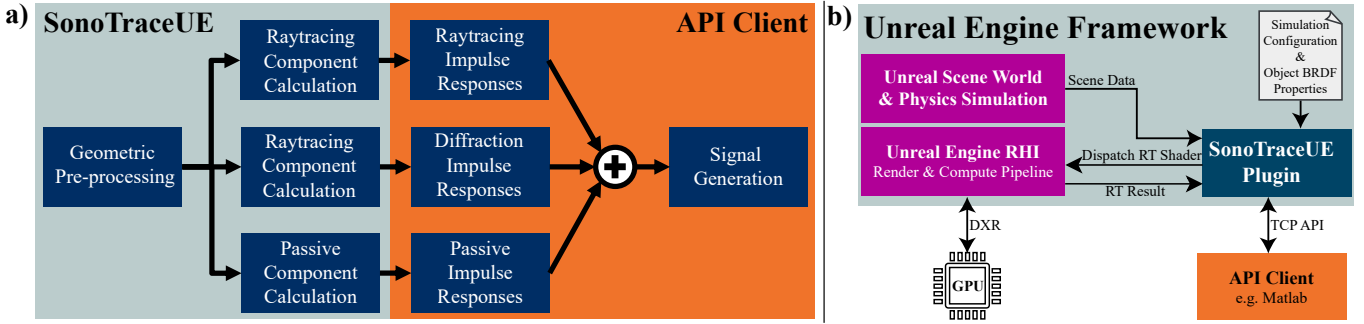


Fig. 3. Diagrams visualizing the architecture of the simulation framework. a) Block diagram showing the sequential stages of the simulation implementation. It shows the three main components: specular, diffraction, and passive sensing, respectively. The impulse response is generated, and the receiver signals are created in third-party software via the TCP API. b) High-level schematic of the proposed system architecture integrated within the Unreal Engine framework. The plugin serves as the main block controlling and executing the simulation pipeline, acting as an intermediary between the host application’s CPU thread, which handles rigid-body physics and dynamic scene updates, and the low-level render dependency graph that uses the Rendering Hardware Interface (RHI) of Unreal Engine to access the GPU. Acoustic propagation is offloaded to the GPU via asynchronous compute shaders utilizing DirectX Ray Tracing (DXR) pipelines. Interaction with the simulation and final signal post-processing is available through a TCP API to third-party software, such as MATLAB.

III. METHODS

This proposed framework is available as open-source and natively supports array configurations of emitters (sources) s and receivers (microphones) m . We will cover all the implementation details in this paper for completeness. Note that some mathematical symbols are different from those in the original SonoTraceLab manuscript.

A. ARCHITECTURE

Figure 1 shows the specific acoustic phenomena our abstraction model handles. As can be seen, refraction and more complex wave transmission are not modeled. Figure 3b shows the flowchart of the simulation. The three main components are shown as specular, diffraction, and passive, respectively. The passive component calculates the direct line of sight between receivers and sound sources (emitters) and is primarily used when simulating passive sensing systems. This figure also shows a clear split between the steps calculated within the Unreal Engine plugin SonoTraceUE and those performed in the external API Client. Currently, we have created one such API Client in MATLAB.

The architecture is further visualized in 3c. The core simulation module, SonoTraceUE, is an Unreal Engine plugin. Unreal is a multi-platform real-time 3D rendering engine, allowing the usage of hardware-accelerated ray tracing using the Unreal Engine Rendering Hardware Interface (RHI). It also has a user-friendly and versatile editor that supports C++ & node-based visual scripting, allowing the user to create large and dynamic acoustic simulation scenarios with support for closed-loop interactions. The plugin retrieves all data required for the scene, including the transformations of all objects and their mesh data. The interaction with the API Client is done over a TCP interface.

B. GEOMETRIC PRE-PROCESSING

In a first offline pre-computation step, all registered objects in the scene are retrieved, and the 3D mesh data is loaded into CPU memory. SonoTraceUE supports both static and skeletal meshes, with the latter capable of animation. During this step, an offline analysis of the scene geometry is performed to identify acoustically significant features, such as edges and holes. As a metric of acoustic significance, a local sharpness or curvature metric is calculated for each i -th triangle T_i of the mesh. First, the discrete mean curvature normal \mathbf{K}_v is calculated for every vertex v utilizing the discrete differential geometry operators defined by Meyer et al. [56]. The scalar mean curvature magnitude is then given by $G_v = \frac{1}{2} \|\mathbf{K}_v\|$.

To robustly detect geometric discontinuities while ignoring smooth surface undulations, we define the curvature variation ΔG_i of the i -th triangle as the range of curvature magnitudes among its adjacent vertices. To ensure consistency across varying mesh resolutions, this metric is modulated by a piecewise-linear area weighting function $w(A_i)$ and a global scaling factor η . The final diffraction curvature metric C_i is defined as:

$$C_i = \eta \cdot w(A_i) \cdot \underbrace{\left(\max_{v \in T_i} G_v - \min_{v \in T_i} G_v \right)}_{\text{Curvature variation } \Delta G_i} \quad (1)$$

As originally proposed and validated in [26], this metric C_i effectively acts as a high-pass geometric filter, responding strongly to sharp edges necessary for diffraction modeling while vanishing on planar or smoothly curved surfaces. From this metric, we calculate two frequency-dependent surface material properties $\beta(T_i, f)$ and $k(T_i, f)$ for each triangle, the opening angle, and the reflection magnitude of the acoustic BRDF, respectively. β governs the angular distribution of the reflected energy, effectively determining the transition between specular and diffuse scattering. At the same time, k represents the frequency-dependent reflection coefficient, scaling the

magnitude of the signal returned from the triangle. To enhance simulation fidelity, the proposed architecture departs from the single-material constraint of prior work. While SonoTraceLab utilized a monolithic material definition for the entire scene mesh, SonoTraceUE supports per-object material granularity. Each geometric primitive in the scene can be linked to a specific acoustic profile.

C. RAY TRACING COMPONENT

To solve the Helmholtz equation in our abstraction model, we separate some phenomena, as visualized in Figure 1. For solving the specular reflections, we use ray tracing. A specified number of rays is emitted into the environment from each emitter source. The rays are distributed using recursive zonal equal area sphere partitioning [57]. For each ray, we calculate the full propagation path. At intersections with an object’s surface, we compute the specular reflection around the surface normal of the triangle T_i that was hit on that mesh. Propagation and specular reflections will continue until either the maximum number of bounces or the maximum propagation length is reached. The ray tracing algorithm is implemented as a compute shader and is dispatched to the Unreal RHI. It uses the DirectX Ray Tracing (DXR) pipeline to perform ray-triangle intersection calculations on ray tracing cores available on modern GPU devices. Algorithm 1 shows a simplified version of the ray tracing algorithm shader. Afterwards, the ray tracing result is parsed further in the SonoTraceUE plugin on the CPU. For each n -th reflection point, a total signal magnitude or strength $M_{rt}(f, n, s, m)$ is calculated over the frequency band f between the sound source or emitter s and receiver (microphone) m . In the following equations, we will omit (n, s, m) for simplicity.

For each receiver m , the total propagation path length r is calculated from the emitter s along this n -th reflection point. With this path length, we can define the geometric spreading loss L_{geo} using the inverse-square law as $L_{geo} = \frac{1}{r^2}$. Atmospheric attenuation $L_{atm}(f)$ is calculated as a function of frequency and total path distance.

The absorption coefficient $\alpha(f)$ is derived linearly and fitted to simulation constants and applied as an exponential decay as $L_{atm}(f) = 10^{r \cdot \alpha(f)}$.

The deviation angle γ is defined as the angle between the ideal specular reflection vector and the actual direction vector to the receiver from the reflection point. Together with the frequency-dependent surface material properties of that triangle, we use that angle to calculate a specular intensity I_{rt} for a given frequency band f as:

$$I_{rt}(f) = \exp\left(\frac{\gamma^2}{2\beta(T_i, f)^2}\right) \cdot k(T_i, f) \quad (2)$$

The magnitude $M_{rt}(f)$ can now be defined as:

$$M_{rt}(f) = L_{geo} \cdot L_{atm}(f) \cdot I_{rt}(f) \quad (3)$$

It is this magnitude that is calculated for each reflection point on the CPU, parallelized across the number of points,

Algorithm 1 Acoustic ray tracing Logic Shader

Input Source Pose P_{source}
Ray Angles Θ
Scene Geometry M (TLAS/BLAS)

Output Hit Data Buffer B

for each Ray Angle $\theta_i \in \Theta$ **do**
 $\vec{p}_{origin} \leftarrow P_{source} \cdot \text{Location}$
 $\vec{d}_{ray} \leftarrow \text{CalculateWorldDirection}(P_{source} \cdot \text{Rotation}, \theta_i)$
 $r_{total} \leftarrow 0$
for $j \leftarrow 0$ **to** $MaxBounces$ **do**
 $H \leftarrow \text{DXR.GenerateRay}(\vec{p}_{origin}, \vec{d}_{ray}, M)$
if $H.isHit$ **then**
 $\vec{d}_{reflect} \leftarrow \text{CalculateReflection}(\vec{d}_{ray}, H.Normal)$
if $j = 0$ **then**
 $r_{total} \leftarrow \text{Distance}(P_{source}, H.Location)$
else
 $r_{total} \leftarrow r_{total} + H.Distance$
end if
 $\vec{v}_{hit} \leftarrow \text{Direction}(H.Location, \vec{p}_{origin})$
 $L_{hit} \leftarrow \text{DXR.GenerateRay}(H.Location, \vec{v}_{hit}, M)$
 $B[i][j] \leftarrow \{H, r_{total}, \vec{d}_{reflect}, L_{hit}\}$
 $\vec{p}_{origin} \leftarrow H.Location$
 $\vec{d}_{ray} \leftarrow \vec{d}_{reflect}$
if $r_{total} \geq MaxDistance$ **then**
break
end if
else
break
end if
end for
end for

and stored in a large point cloud data structure within the framework. As described in the architecture, the next steps are performed in a third-party client after transferring the data via the TCP API. With this point cloud data, which contains all magnitude values for the reflection points, we can create the complete transfer function that encodes the specular, absorption, and diffusion acoustic phenomena in our simulation model. This transfer function $H(f)$ is calculated as follows:

$$H(f) = M_{rt}(f) \cdot e^{j \cdot \frac{\omega}{c} \cdot r} \quad (4)$$

with the second term defining the signal delay by the path propagation and c the speed of sound set to 343 m/s. This complex transfer function can now be transformed into the time domain using an inverse Fourier Transform \mathcal{F} :

$$h(t, n, s, m) = \mathcal{F}^{-1}\left[H(f, n, s, m)\right] \quad (5)$$

For calculating the final impulse response $h_{s,m}(t)$ for the m -th receiver and coming from emitter s , one has to sum up the impulse responses for the N reflection points in the scene as calculated by the ray tracing shader:

$$h_{s,m}(t) = \sum_{n=1}^N h(t, n, s, m) \quad (6)$$

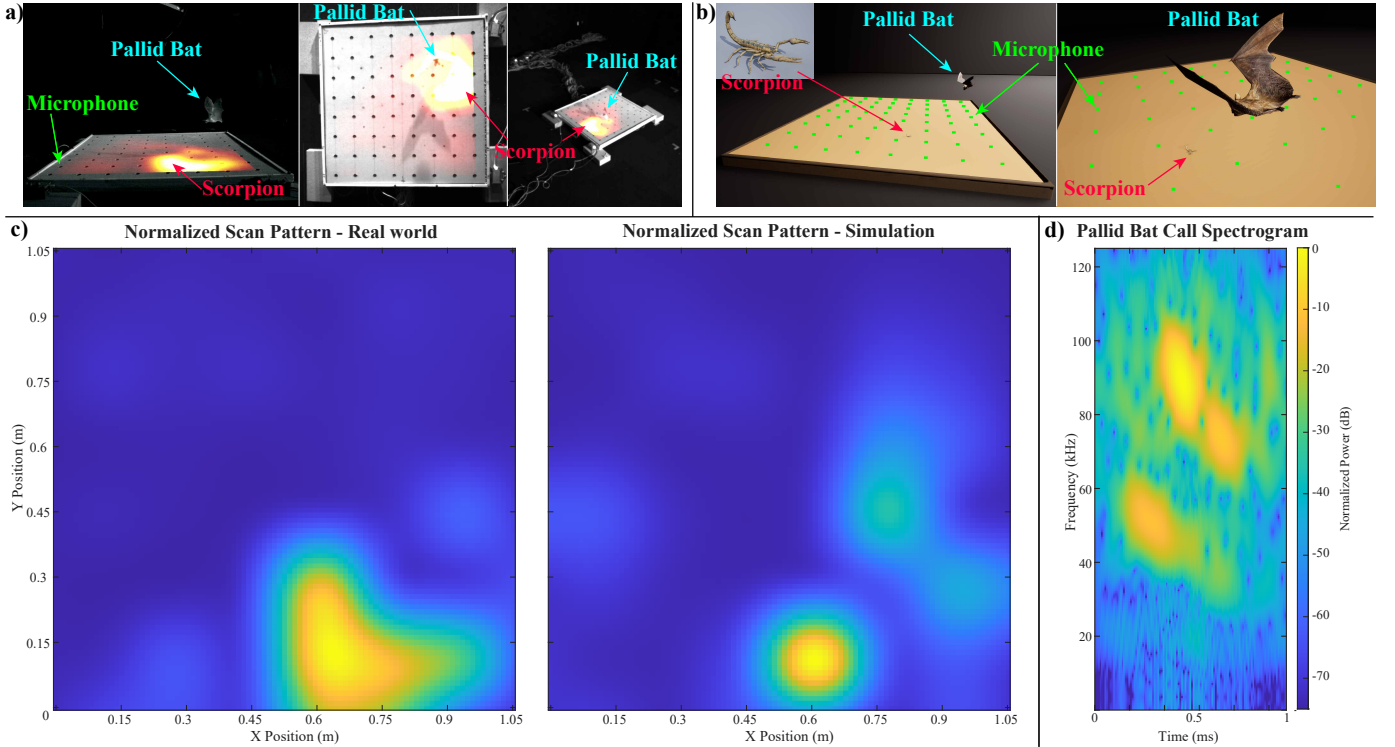


Fig. 4. Comparison of the real-world experimental data of a single frame and its simulated recreation of the pallid bat hunting behavior. a) Three camera views captured simultaneously of the bat approaching its scorpion prey in the real-world experiment. This scorpion is sitting on a flat surface, with the 64-microphone array embedded within it. The acoustic intensity of the echolocation (scan pattern) is shown in a color gradation overlay. b) The same frame recreated with SonoTraceUE in Unreal Engine with the same poses for the microphones, scorpion, and bat. The locations of all 64 microphones are shown with green dots. A close-up of the 3D model used for the scorpion is shown in the top-left corner. c) The normalized scan patterns showing the acoustic intensity across the array. It shows the attention zone of the bat’s emitted call. While the location is the same for the real-world and simulated results, the emission directivity influences the visible pattern. d) The spectrogram of the echolocation signals during this measurement frame of the approaching bat, used by the simulation.

D. DIFFRACTION COMPONENT

The ray tracing component is only valid for larger Helmholtz numbers. Diffraction would require a large number of rays, which would be computationally unfeasible. To still have a fast solution for modeling this component, we proposed in SonoTraceLab a Monte Carlo approximation based on the local curvature values C_i calculated during the pre-compute step to identify a fixed number of high-local-curvature diffraction echo candidates. The same technique is applied here.

First, we sort all triangles T_i based on their curvature values C_i . Subsequently, we use importance sampling to distribute a fixed number of diffraction candidates per mesh across its geometry, where the probability of generating a point on a specific triangle is proportional to its curvature [58]. To avoid aliasing artifacts in the probability distribution, a small amount of dithering noise is applied during construction of the Cumulative Distribution Function (CDF). Only meshes that are within the field of view or frustum of the emitter source s as defined in the configuration of the simulation are candidates for diffraction. Next, the candidates are filtered based on having line-of-sight to the sound source s and a configurable incidence-angle constraint based on the angle between the triangle candidate’s surface normal and the vector

to the sound source. Afterwards, a similar approach is followed as in the previous section for calculating the magnitude $M_d(f)$ for the o -th diffraction points of the remaining candidates O . First, we calculate the path r between the source s , receiver m , and the o -th diffraction point. The magnitude $M_d(f)$ can now be defined as:

$$M_d(f) = L_{geo} \cdot L_{atm}(f) \cdot I_d(f, T_i) \quad (7)$$

with $I_d(f, T_i)$ a specific material diffraction coefficient. This method models the diffraction point as a secondary omnidirectional point source, rather than a direction-dependent reflection. The simulation of the diffraction component is implemented using parallel gathering of diffraction candidate points, enabling concurrent multi-core execution that substantially reduces computation time, even for large, high-resolution scenes with many candidates, while remaining optimized compared to SonoTraceLab.

The synthesis of the transfer function $G(f)$ in the third-party client can now be done similarly to that of the specular component:

$$G(f) = M_d(f) \cdot e^{j \frac{\omega}{c} \cdot r} \quad (8)$$

This complex transfer function can now be transformed into

the time domain using an inverse Fourier Transform \mathcal{F} :

$$g(t, o, s, m) = \mathcal{F}^{-1} \left[G(f, o, s, m) \right] \quad (9)$$

The final impulse response $g_{s,m}(t)$ for the m -th receiver and coming from emitter s requires us to sum the impulse responses:

$$g_{s,m}(t) = \sum_{o=1}^O g(t, o, s, m) \quad (10)$$

E. PASSIVE COMPONENT

A new optional component has been added to the proposed method, which calculates direct propagation between the source and receiver, which can be useful for simulating passive systems, a feature not available in the original SonoTraceLab. This feature is implemented by performing a line-of-sight test between each source s and receiver m , and calculating the propagation distance r between them.

The configuration scaler parameter $I_p(f)$ defines the initial source magnitude. $M_p(f)$ can now be defined as:

$$M_p(f) = L_{geo} \cdot L_{atm}(f) \cdot I_p(f) \quad (11)$$

Then we can synthesize the transfer function $P(f)$ as follows:

$$P(f) = M_p(f) \cdot e^{j \cdot \frac{\omega}{c} \cdot r} \quad (12)$$

This complex transfer function can now be transformed into the time domain using an inverse Fourier Transform \mathcal{F} to get the final impulse response :

$$p_{s,m}(t) = \mathcal{F}^{-1} \left[P(f, s, m) \right] \quad (13)$$

F. SIGNAL GENERATION

With all partial components calculated, we can generate the scene's total spatial impulse response $h_s(t)$ by simply summing up the partial solutions for each sound source s . In the original SonoTraceLab system, an additional post-processing step was implemented to model, for example, the biological system's reception and emission organs.

For humans, this is called the Head-Related Transfer Function (HRTF); for echolocating species, it is called the Echolocation-Related Transfer Function (ERTF), which is the product of the emission pattern and the HRTF. No modifications were made to this method, and it is available in the third-party API client for post-processing. For a more detailed description of the implementation of these filters, we refer to the original publications [59], [26].

Now, with assuming a signal $s_e(t)$ emitted by the source s , we can calculate the signals arriving at a receiver r as follows:

$$s(t) = h_s(t) * s_e(t) \quad (14)$$

IV. EXPERIMENTAL RESULTS AND VALIDATION

The original work of SonoTraceLab was numerically validated in several bioacoustic scenarios [26]. In this section, we will focus the experiments on the new aspects and changes introduced into SonoTraceUE and provide example practical applications of the simulation framework, with a focus on supporting larger scenes with more dynamic applications and on closed-loop testing. Note that a comparative analysis with other simulation frameworks was outside the scope of this work due to the unique positioning of the proposed system. Existing commercial solvers are not always readily available for purchase. Furthermore, the absence of standardized formats for input configurations and output results precludes reliable, reproducible benchmarking of specific experimental scenarios across disparate software ecosystems. All experiments were run on a laptop with an NVIDIA RTX 3080 Ti Laptop GPU (16 GB) and an Intel i9-12900HK CPU with 32 GB of memory.

A. BIOACOUSTICS

In a first experiment, we used SonoTraceUE to simulate a biological acoustic system, specifically pallid bats (*Antrozous pallidus*). Verreycken et al. performed a study of their hunting behavior where they were trained to hunt for a scorpion (*Hadrurus arizonensis*) that was placed on a random position within a planar microphone array with 64 microphones [60]. This array could record the bats' echolocation call sequences while they searched, approached, and eventually caught the scorpion. By analyzing the bat call's acoustic intensity at each microphone, one can see the bat's attention point and its shape. We recreated this scenario in simulation using the same recorded call as the emitted signal within a specific measurement frame. The microphone array locations and the 3D position and rotation of the bat were recreated from the study data, including the bat's flight path data. In this scenario, we used only the passive component of the simulation. The results can be seen in Figure 4. As seen in the acoustic intensity scan pattern heat maps, the attention location matches that of the study. Still, the specific shape is not reproduced because the pallid bat's physical emission pattern was not modeled or simulated. This experiment validates the system's geometric accuracy by confirming that the simulated time-of-arrival data aligns with real-world array recordings. Furthermore, the ability to easily use external study data in a visual 3D editor, such as the exact flight paths, represents a significant workflow improvement. By enabling the simulation of passive-listening scenarios, SonoTraceUE expands the scope of potential research beyond active echolocation to include passive sensing, capabilities previously unsupported.

In a second experiment, we tested the framework's ability to allow further insight into how these species use echolocation in their natural habitats. In the same study by Verreycken et al., additional measurements were conducted in which the surface supporting the microphone array was varied between a wooden flat surface and a layer of pebbles, the latter representing a rough surface. Subsequently, they compared

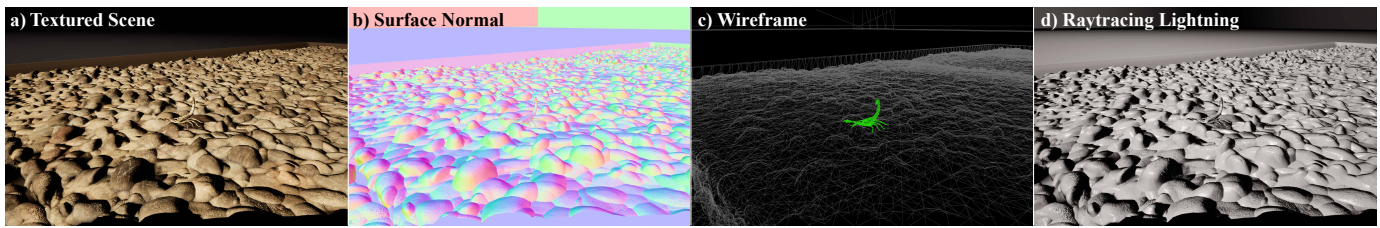


Fig. 5. Various visualizations of the 3D scene from the same point of view used during the bioacoustic surface analysis experiment in simulation. The experiment shows how a rough surface affects the acoustic signature of a scorpion during bat echolocation hunting. a) A close-up of the 3D scene as created in Unreal Engine. b) The surface normal is visualized, which is used by the proposed method for calculating the curvature of the 3D meshes. c) The wireframe of the 3D meshes used in the scene showing the triangle-based geometry with the scorpion highlighted in green. d) Only the light rendering result is shown here, where Unreal Engine also uses hardware-accelerated ray tracing to simulate light bouncing throughout the scene.

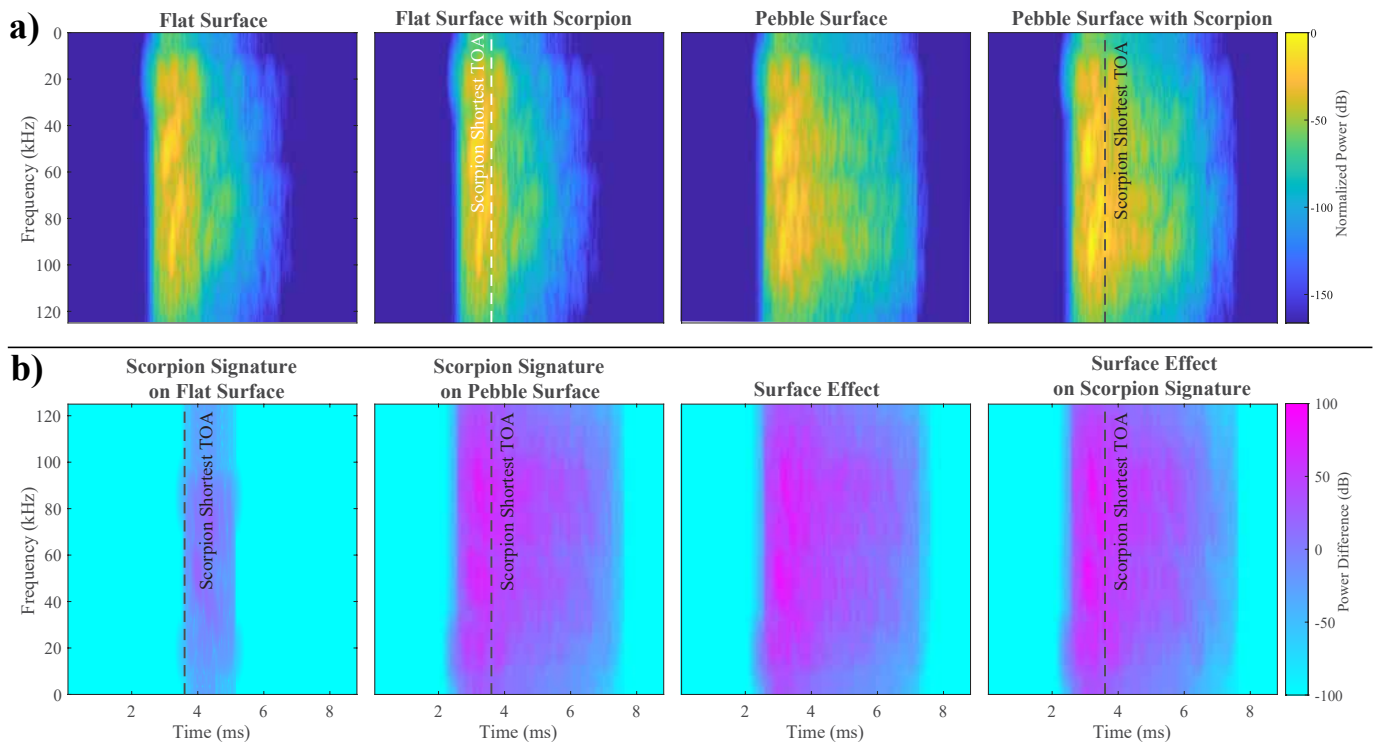


Fig. 6. Spectrogram results of the bioacoustic surface analysis experiment in simulation to show the surface effect on the scorpion's acoustic signature when it is hunted by a bat that uses echolocation. We also add a vertical line marking the first arrival of the echo that reflects on the scorpion itself when it was present in the scenario. a) These baseline spectrograms show the four distinct scenarios that were simulated from left to right: a flat surface baseline, a flat surface with target scorpion, a pebble surface baseline, and a pebble surface with target scorpion. b) Difference spectrograms that isolate the effects of the surface and/or scorpion on the echolocation acoustic signatures for the pallid bat. From left to right: The scorpion's acoustic signature (flat w. scorpion - flat), the scorpion's acoustic signature as influenced by specular reflections on the pebbles (pebbles w. scorpion - pebbles), the surface effect of the pebbles (pebbles - flat), the surface effect of the pebbles when scorpion is present (pebbles w. scorpion - flat w. scorpion).

the level of focus during the call for both surface types and analyzed echolocation precision. The degree of sonar beam focus was higher, and the distribution of centroid distances to the scorpion prey was shorter for the flat wooden surface. This supported the assumed theory that the prey camouflage themselves by living on rougher surfaces, such as the pebbled surface [61]. SonotraceUE now allows us to simulate and numerically determine the effect of the surface on the scorpion's acoustic signature. This scenario was recreated using 3D modeled pebbles[62] and can be seen in Figure 5. We used the same position for the pallid bat as in the previous experiment, and the same call was recorded by the surface microphones.

We simulated both the specular and diffraction components in this experiment using 600 000 initial rays that could bounce at most 2 additional times, and set the number of frequency bins to 14. To simulate these four scenarios, on average, the geometric pre-processing took 270.54 ms while the simulation of the specular and diffraction components took 471.28 ms and 1025.13 ms respectively.

Figure 6a shows the spectrogram results of this experiment, where we are varying the surface (flat vs. pebbles) and the presence of the target (scorpion vs. no scorpion). This arrangement yields four distinct measurement scenarios: (1) a

flat surface baseline, (2) a flat surface with target scorpion, (3) a pebble surface baseline, and (4) a pebble surface with target scorpion. Furthermore, to gain further insight into the pebbles' surface effects and acoustic signatures, we created difference spectrograms for these scenarios, shown in Figure 6b, which clearly show the scorpion's signature and the effect of surface reflections on it. It further supports the theory that the surface effect helps camouflage the scorpion by altering its acoustic signature, while still allowing the bat to find its prey even on rougher surfaces by making multiple passes along the same surface from different angles.

The simulation of the specular components provides clear evidence that increased surface roughness introduces significant scattering noise, almost completely masking the prey's deterministic acoustic signature. This level of environmental fidelity highlights SonoTraceUE's critical advantage in handling scene complexity and simulating the diffraction and scattering effects of hundreds of pebbles in less than 2s. With the proposed system, we can achieve large scenes with the mesh density required to resolve our scene's Helmholtz number, ensuring that sub-centimeter environmental features are treated as acoustically significant rather than mere surface roughness.

B. CLOSED-LOOP ROBOTICS WITH ACOUSTIC SENSING

In a second series of experiments, we tested human-made acoustic systems to validate the usage of the proposed framework for closed-loop robotics applications. We recorded an indoor dataset using a 3D sonar sensor [63], an RGB camera, and a high-resolution LiDAR sensor mounted on a small mobile platform. The scene was an office lobby with objects such as benches, vending machines, radiators, trash bins, and (elevator) doors.

The goal was to use the acoustic sensor to create the mobile platform's trajectory. The camera and LiDAR sensor served as high-resolution groundtruth sensors. We created this trajectory in two steps: first, the system used acoustic odometry to estimate the motion of a mobile agent by decomposing the mobile platform's speed into linear and rotational components [64]. In a second step, we ran BatSLAM, a bio-inspired Simultaneous Localization and Mapping (SLAM) algorithm where we use 3D acoustic images from the sonar sensor to estimate the position of the robot [65], [66]. The correlation between acoustic images is continuously calculated to perform loop closure detection, which indicates recognition of previously visited places and helps minimize error in the trajectory mapping, as in acoustic odometry.

The goal of these experiments is to repeat them in a simplified virtual 3D recreation of this real environment, using the same acoustic sensor simulated with the proposed method, and to compare the acoustic odometry and SLAM results. The real-world scene and its virtual counterpart are shown in Figure 8 along with the sensor setup. The overall shape and layout of the real office lobby were recreated from 3D-scanned LiDAR data, with high-definition 3D models placed for several objects, as mentioned earlier.

The hypothesis is that this simplified building geometry, combined with the unique acoustic signatures of the various high-resolution objects, will yield performance comparable to that in closed-loop robotic simulation with acoustic sensor systems.

The LiDAR sensor serves as the groundtruth reference and was used as input to PIN-SLAM[67], a state-of-the-art LiDAR SLAM algorithm to generate a trajectory map.

From this trajectory, the correct 3D poses of the acoustic system were calculated in a closed-loop simulation scenario within the simulated scene. The acoustic system consists of a single emitter transmitting a 2.5 ms broadband chirp call between 25 kHz and 50 kHz, and a 32-element planar microphone array. Both the specular and diffraction components in this experiment were enabled with 80 000 initial rays that could bounce at most 2 additional times, and the number of frequency bins was set to 14. The offline computational cost of the geometric pre-processing was 300 ms. At the same time, during a single simulation frame, the specular and diffraction components took 516.26 ms and 874.21 ms, respectively, on average.

For creating the acoustic odometry results, we follow the same methodology as detailed in [64]. Both simulated and real acoustic signals were converted into 2D acoustic images representing the horizontal plane in front of the mobile platform, with a resolution of 0.5° spanning -80° to 80° . The results of the acoustic odometry trajectories can be seen in Figure 7a. Both the real and simulated acoustic sensors exhibit drift relative to the LiDAR groundtruth in both straight lines and corners. The simulation recreation does not perfectly mirror the stochastic drift path of the real data. However, to validate that the proposed simulation framework can be used to simulate such acoustic systems and their applications, such as acoustic odometry, we also correlated the errors between real and simulated velocity estimations, as shown in Figure 7b.

These results show that there is a high correlation in residuals for both rotational and linear velocity estimation, with the first one being extremely similar. The simulation and real datasets exhibit peak errors in the same geometric scene areas. The mean rotational velocity error difference between the real and simulated acoustic odometry result was 1.38° with a standard deviation of 3.36° , while the same for the linear velocity resulted in a mean of 0.037 m/s with a standard deviation of 0.076 m/s. We believe the larger difference in linear velocity is because of more reflections being present in the real-world because of surface imperfections that we did not model in our simplified virtual re-creation. This demonstrates that, even though the resulting acoustic odometry trajectory does not match well, the simulated robotic application exhibits behavioral failure alignment with the real-world.

To further assess the fidelity of the simulation, we evaluated the performance of the BatSLAM place recognition as described in [65] on the same datasets. Central to this bio-inspired SLAM algorithm is the ability to recognize previously visited locations by correlating current acoustic images with a history of previous ones. We replicated this process by

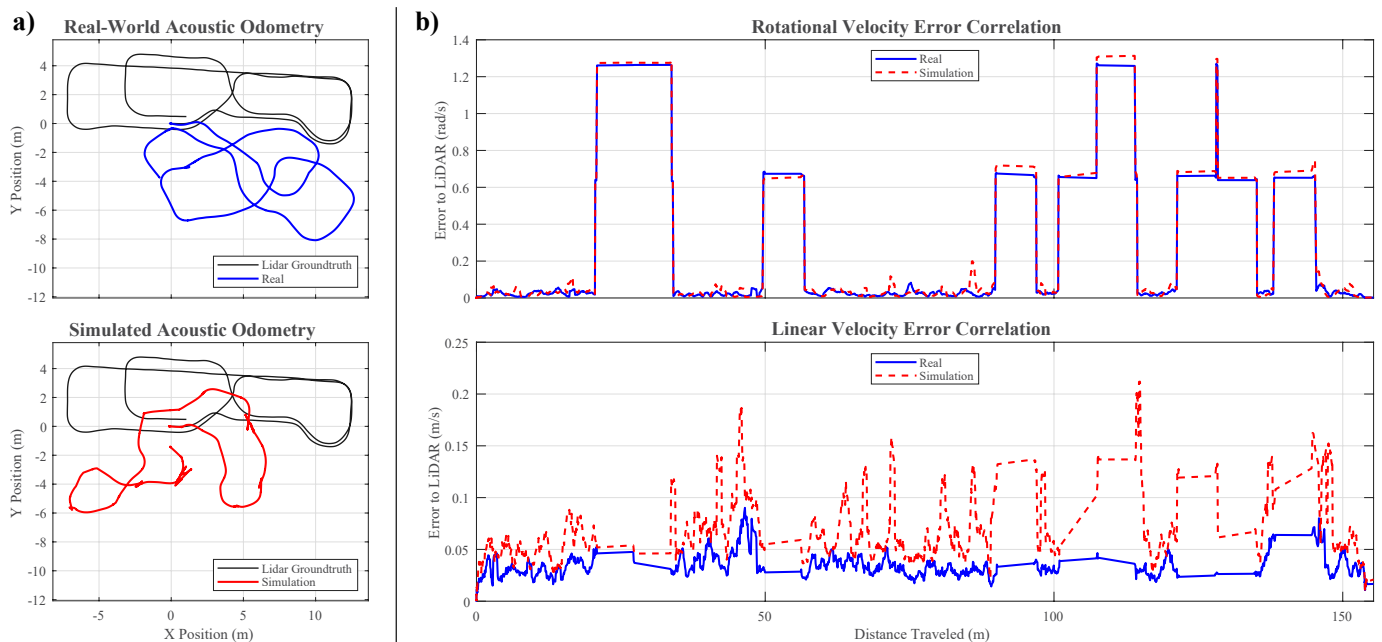


Fig. 7. Results of the acoustic odometry for the robotics experiment. a) The trajectories of the real and simulated 3D sonar sensors compared to the groundtruth as generated by a LiDAR sensor. There is a clear difference in the resulting acoustic odometry trajectory. b) The rotational and linear velocity as calculated by the acoustic odometry, as compared to that from the LiDAR groundtruth represented as an error calculation. This shows the correlation between the real and simulation data, where the acoustic odometry fails to accurately estimate these velocities: the rotational velocity estimates are almost identical, and the linear velocity estimates are similar, albeit with a larger error margin. We believe this is because of more reflections being present in the real-world because of surface imperfections that we did not model in our simplified virtual re-creation.

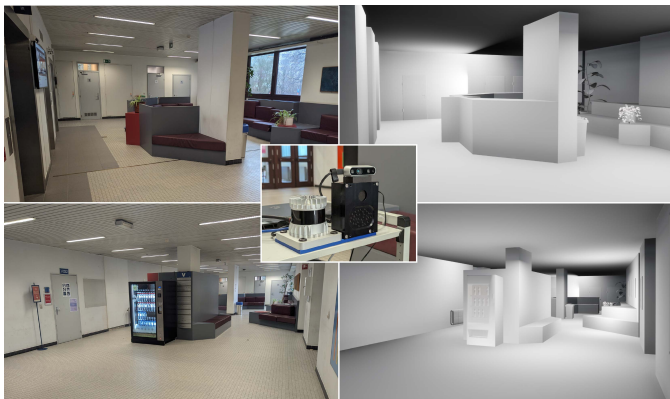


Fig. 8. The robotics experiment within an indoor office lobby shown with real photos on the left and the virtual simplified recreation in Unreal Engine from the same point of view on the right. The photo in the middle shows the sensor configuration used for generating the dataset, including the 3D imaging sonar sensor [63], the Ouster OS0-128 LiDAR, and the Intel RealSense D435i camera.

generating pairwise-difference matrices for both the real and simulated trajectories, as shown in Figure 9a. A direct comparison of these matrices reveals a high degree of structural alignment, with the simulation successfully predicting the distinctiveness of key environmental features when revisiting certain locations. In Figure 9b, we quantified this alignment by calculating the structural discrepancy between the real and simulated domains, yielding a mean residual difference of 0.0745 and a standard deviation of 0.112. These low error

metrics indicate that the simulation preserves the perceptual uniqueness of the environment, ensuring that loop closure candidates appear consistently in both domains. Consequently, this validates the proposed framework as a reliable testbed for developing and fine-tuning acoustic place recognition algorithms. If we apply the template matching in the full BatSLAM algorithm, we get the resulting trajectories as seen in Figure 10.

C. COMPUTATION ANALYSIS

To demonstrate the scalability and real-time capabilities of the proposed SonoTraceUE framework, we conducted a comprehensive computational performance analysis. The evaluation's primary objective was to quantify the system's resource utilization and execution latency across varying degrees of scene complexity and simulation fidelity.

Specifically, we investigated the impact of increasing geometric density, measured in triangle count, on both memory footprint and compute time during the mesh preparation step. Furthermore, we analyze the runtime performance of the specular and diffraction components under increasing computational load, isolating the effects of increasing ray counts, receiver and emitter densities, the number of allowed bounces, and diffraction parameters. These metrics provide insight into the algorithmic efficiency of the hardware GPU-accelerated pipeline and establish the operational boundaries for real-time acoustic simulation in large-scale environments.

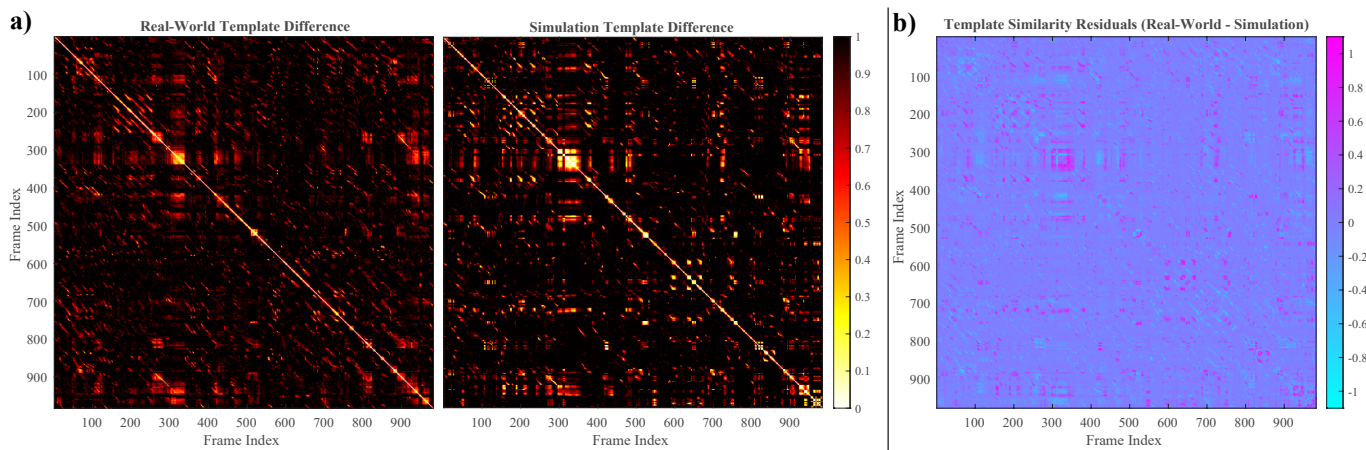


Fig. 9. Results of the acoustic image template matching for the (Bat)SLAM application. a) The difference matrices between all frames of the real 3D sonar acoustic images on the left, and the simulated sensor on the right, respectively, along the full trajectory of the dataset. b) This shows the difference between the previous two matrices to show the residuals between them. The mean difference between real-world and simulation template matching was 0.0745 with a standard deviation of 0.112. Based on these metrics and the visual comparison, the template-matching results clearly show a high correlation across real-world and simulated scenarios, demonstrating that this application can be validated and tested in simulation.

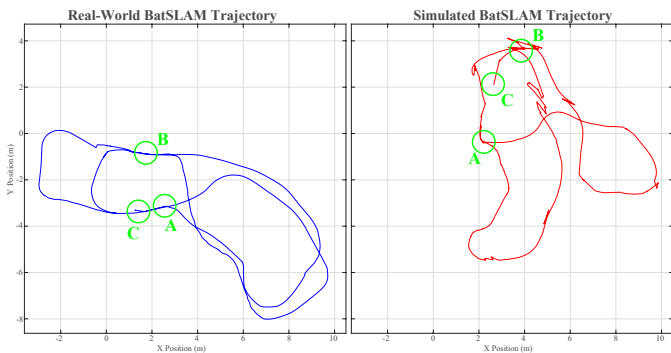


Fig. 10. BatSLAM trajectory reconstruction integrating acoustic odometry with template-based loop closure detection. Three distinct loop closure zones are annotated as A, B, and C. a) The real-world trajectory successfully registers loop closures in all three zones, effectively mitigating cumulative odometry drift and preserving the global topological shape. b) The simulated trajectory successfully identifies loop closures at A and B but fails to register a detection at zone C. The lack of correction at C results in uncorrected drift and significant deviation from the groundtruth path topology.

For a first analysis, we looked at the first geometric pre-processing step, which happens offline before the simulation starts. It calculates the curvature for each triangle of the 3D scene as well as the BRDF properties for each triangle and frequency bin combination as detailed in Subsection III-B. The memory footprint of the data stored in memory is equal to $128 + 8 \cdot T(12 + F)$ bytes, where T is the triangle count and F is the frequency bin count.

In this experiment, we scaled the triangle count in powers of two from 1 to 2^{26} and the number of frequency bins from 1 to 20, and ran five runs with all combinations of triangle count and frequency resolution. Firstly, we examine computational scaling with increasing geometric complexity (increasing triangle count) for both computation time and memory usage when saving the calculated curvature and

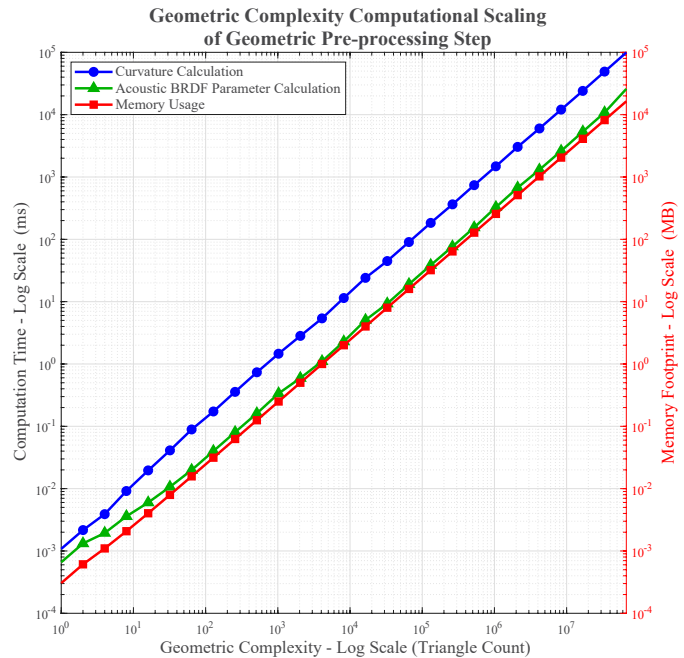


Fig. 11. Computational scalability of the offline pre-processing stage as a function of geometric complexity defined by the triangle count. The graph decomposes the processing latency into purely geometric curvature estimation and frequency-dependent acoustic BRDF parameter mapping, and also shows the memory footprint. The data represent the mean of five execution runs with a fixed high-fidelity spectral resolution of 20 frequency bins. The results confirm linear scalability for both compute time and memory.

BRDF data. The mean across these five runs is shown in Figure 11 for a fixed frequency resolution of 20 bins, in a worst-case scenario. We observe a maximum memory usage of 16384 MB and computational times of 99.43 s and 25.91 s for the curvature and BDRF parameter calculations, respectively. All aspects scale linearly, as expected. Secondly, the same analysis was done for scaling with the frequency bin resolution

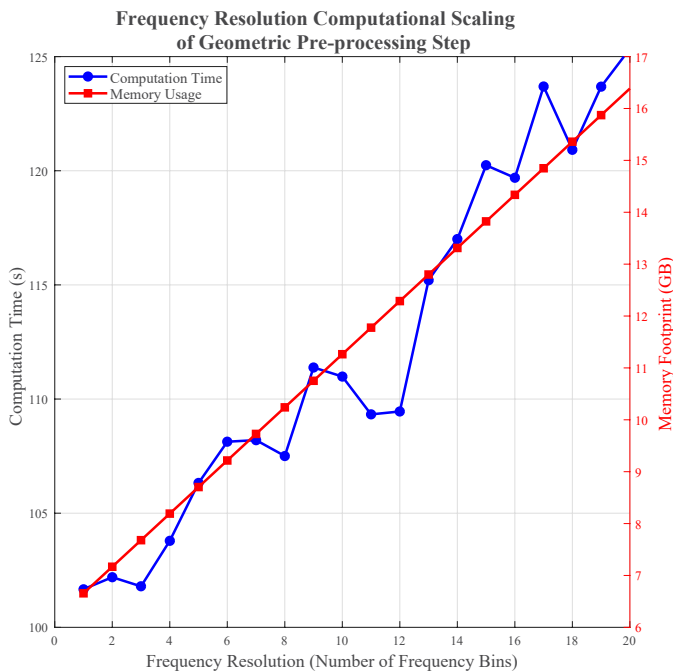


Fig. 12. Impact of the spectral resolution defined by the number of frequency bins on resource utilization for a fixed high-density mesh of 2^{26} triangles. This demonstrates that increasing simulation fidelity, by increasing frequency resolution, imposes a proportional linear cost on pre-processing time and memory requirements.

and is shown in Figure 12 for a fixed geometric complexity resolution of 2^{26} triangles, in a worst-case scenario, showing a similar linear scaling. Since this step is performed once before the simulation starts, these results indicate that even for very large, dense geometric scenes with high spectral resolution, the additional simulation resource utilization remains reasonable.

Following geometric pre-processing, the main simulation loop consists of three sequential stages: ray tracing shader execution, specular component simulation, and diffraction component simulation. We first analyze the execution time and GPU memory usage of the ray tracing shader. In this experiment, the number of initial rays was scaled in powers of two from 1 to 2097152 (2^{21}), while the number of specular bounces varied between 1 and 10. Five runs were performed for every combination to capture the variance. To stress-test the system, the scene setup ensured that every ray completed the maximum number of bounces.

Figure 13 illustrates the results, where the shaded region represents the variability between the minimum (1 bounce) and maximum (10 bounces) configurations, and the solid line indicates the mean. Memory usage scales linearly with the number of initial rays and bounces, as expected. Computation time follows a similar linear trend initially but exhibits exponential behavior beyond approximately 65536 initial rays. The Unreal Engine and DXR documentation do not offer any further insight into why this occurs with these large ray counts. We speculate this may not happen on larger High-Performance Compute (HPC) platforms with more available GPU resources.

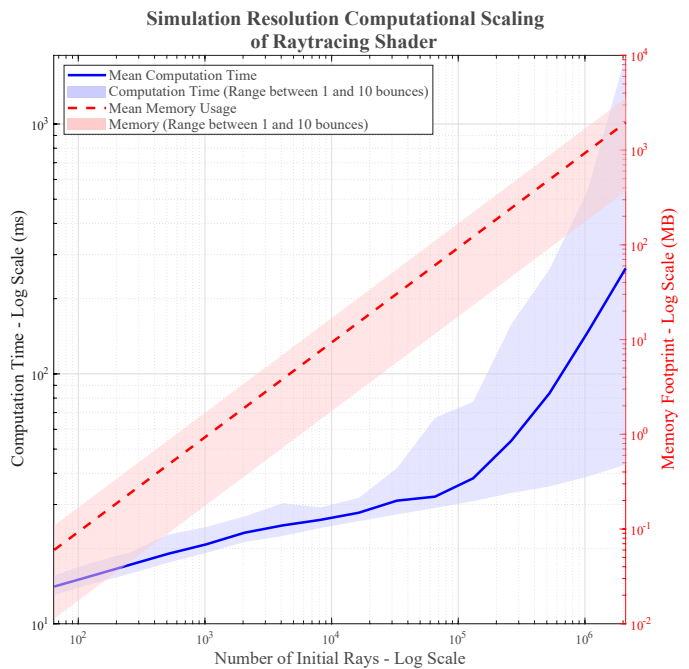


Fig. 13. ray tracing shader performance scaling with initial ray count. The solid line represents the mean execution time across all bounce depths, while the shaded region indicates the range between the minimum (1 bounce) and maximum (10 bounces) workload. The secondary axis tracks the GPU memory utilization. The number of initial rays was scaled in powers of two from 1 to 2^{21} .

For the maximum load of 2^{21} initial rays with 10 bounces, we observed a computation time of 1882.02 ms and a memory usage of 3536 MB. While useful for benchmarking, simulating this number of rays and specular reflection points exceeds the practical memory constraints of typical workstations when also simulating the specular magnitude of each point in the next step, restricting such scenarios to HPC environments.

Upon completion of the ray tracing shader, the reflection points are parsed on the CPU to compute the specular and diffraction components. Beyond the raw point count, the computational load depends on several scaling parameters: the number of sources (S), the number of receivers (R), and the number of frequency bins (F). We define the product of these terms as the simulation complexity. Both specular and diffraction components scale with a complexity of $\mathcal{O}(N \cdot S \cdot R \cdot F)$, where N represents the number of simulation points. Parallelization across N threads reduces computation time proportionally to the number of available CPU cores. A comprehensive parameter sweep was conducted, with five runs per combination. The parameter ranges were constrained as follows: points from 1 to 1048576 (2^{20}), sources from 1 to 32, receivers from 1 to 1024, and frequency bins from 1 to 20. Note that we did not run any combination that exceeded 20 GB of memory due to limitations of the test system. Figure 14a presents the performance landscape for the specular component as an interpolated logarithmic plot, mapping average execution time against complexity and point count. Figure 14b illustrates the corresponding landscape for the diffraction component. The

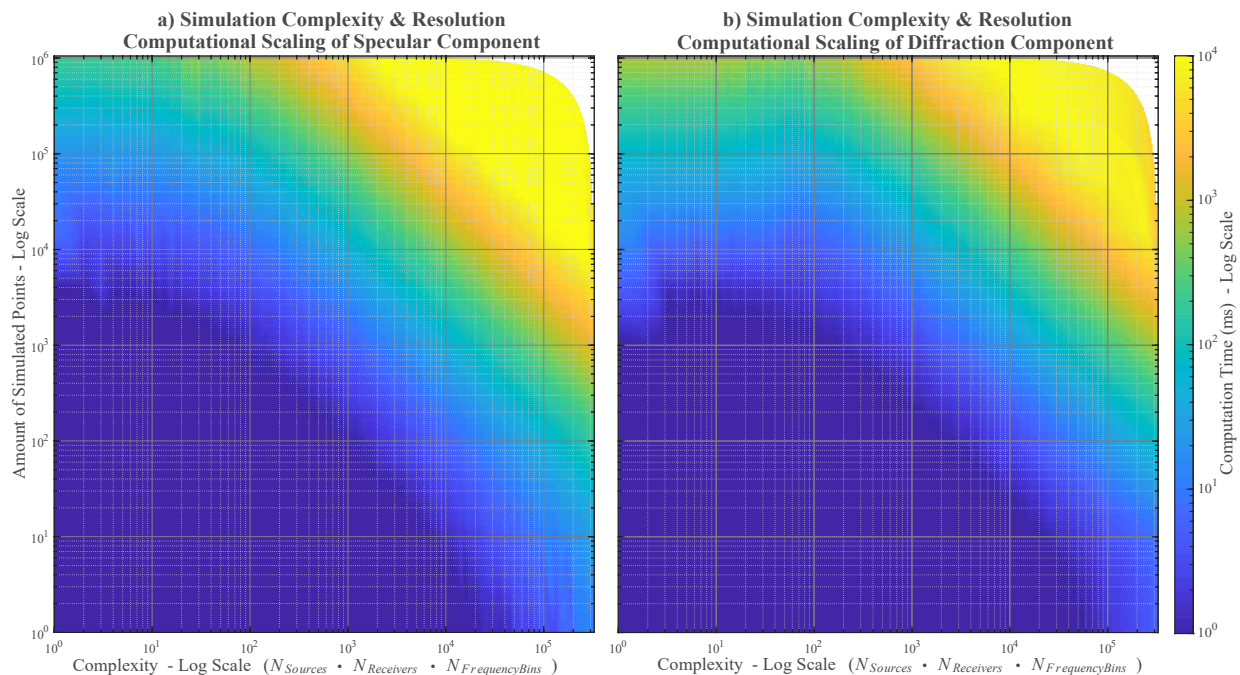


Fig. 14. Computational performance landscape of the simulation components. The heatmaps illustrate the scaling of execution time with simulation complexity and the number of simulation points. a) Shows this computational landscape for the specular component. b) Shows this computational landscape for the diffraction component.

worst-case computation we found was 32.88 s with 2^{20} , 2^{18} points and a simulation complexity of 13 312 (16 emitters, 64 receivers, and 13 frequency bins). Finally, Figure 15 details the peak memory usage, which is consistent across both specular and diffraction stages. The worst-case memory usage found was 19 585 MB with 2^{20} points and a complexity of 3200 (5 emitters, 64 receivers, and 10 frequency bins).

V. CODE AVAILABILITY AND USAGE

We made the simulation framework available under <https://github.com/Cosys-Lab/SonoTraceUE> [68]. The source code is provided as a complete Unreal Engine project containing the SonoTraceUE plugin and a few example scenarios. These examples help users get started efficiently. As mentioned in Subsection III-A, the signal generation is available via a TCP API in an external third-party client. It is currently implemented as an open-source MATLAB Toolbox under <https://www.mathworks.com/matlabcentral/fileexchange/183020-sonotraceue-matlab-toolbox> [69]. The workflow leverages the client-server architecture. First, the user opens the provided Unreal Project, where the 3D scene is defined. Unlike the previous MATLAB-only implementation, which loads meshes via a script, the environment is now configured directly within the Unreal Editor. This allows for visual placement of the sensor and emitter actors, as well as the assignment of acoustic material properties to objects using the editor’s native interface. Furthermore, entire world simulations and dynamic scenarios can be scripted within the Unreal framework. Once the scene is prepared, the simulation is started within the engine, initializing the simulation and the API TCP server. On the client side, the user utilizes

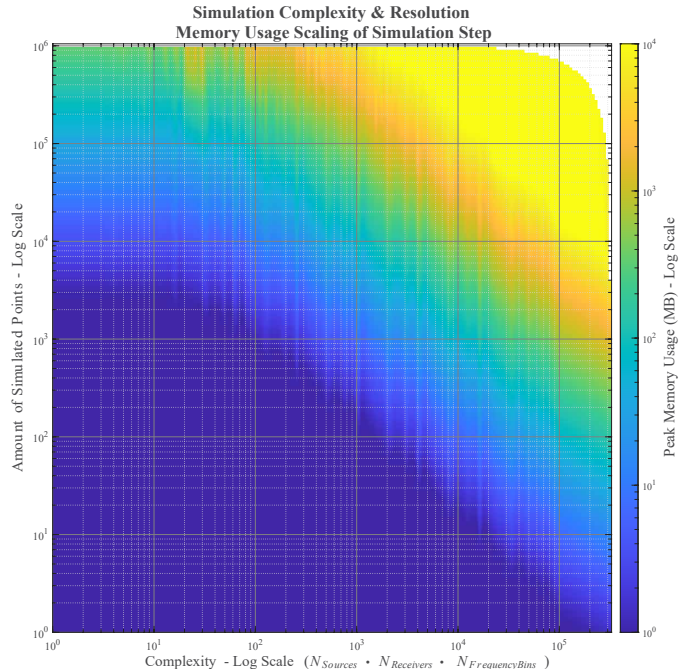


Fig. 15. The memory footprint scaling for the CPU-based simulation components. The memory footprint for specular and diffraction is the same when using the same complexity input parameters. The heatmap visualizes memory requirements relative to simulation complexity and the number of active simulation points, highlighting the constraints in high-fidelity scenarios.

the provided MATLAB toolbox to interact with the running simulation. The user establishes a connection to the server to retrieve the simulation configuration. The user can trigger the simulation via the API and control the sensor's position or the position of its parent mobile system. The engine performs a hardware-accelerated simulation and returns the resulting point cloud containing all simulation data over the TCP connection, which can then be further processed.

VI. CONCLUSION

In this paper, we present SonoTraceUE, a novel high-fidelity acoustic simulation framework implemented as a plugin for Unreal Engine. Building upon the theoretical foundation of the previous work, SonoTraceLab, this new architecture transitions from a MATLAB-based solver to a hardware-accelerated, real-time 3D engine. By leveraging hardware-accelerated ray tracing for specular reflections while keeping the curvature-based Monte Carlo approximation for diffraction, SonoTraceUE addresses the critical scalability and latency limitations of its predecessor. We demonstrate the framework's validity through a series of bioacoustic and robotic experiments, showing that it can accurately reproduce the relevant acoustic cues of biological echolocation and generate synthetic data that can drive closed-loop robotic navigation algorithms, such as BatSLAM.

While SonoTraceUE significantly advances the state of geometric acoustic simulation, it is not without limitations. First, as with all geometric approaches, it remains an approximation of the Helmholtz equation. While it offers a computationally tractable alternative to wave-based solvers (FEM/BEM) for high-frequency, large-scale environments, it cannot fully replace exact numerical methods for low-frequency or small-scale bounded problems. Second, the current implementation of the diffraction model relies on a local curvature metric. This approach prioritizes computational efficiency over full principal curvature computation because Unreal Engine's mesh interface does not provide complete one-ring neighborhood information.

Consequently, this approach requires meshes with adequate tessellation density at acoustically significant features to ensure that the per-triangle curvature variation accurately captures local geometry. Furthermore, because the curvature calculation is performed offline, animated skeletal meshes are not supported for the diffraction component calculation. We also see potential to extend the hardware-accelerated pipeline to further offload workloads to the GPU, for example, by integrating real-time geometric curvature analysis and the entire specular magnitude calculation within the compute shaders.

Looking ahead, several avenues for further development are planned to enhance the framework's fidelity and accessibility. Future iterations will expand the ray tracing shader to include acoustic transmission and refraction, enabling the simulation of multi-medium environments such as underwater acoustics or sound propagation through complex thin-walled structures. Additionally, to further reduce latency for real-time closed-loop applications, we aim to integrate accelerated C++ math

and digital signal processing libraries, such as optimized FFT implementations, directly within the plugin to minimize overhead during signal synthesis caused by the current TCP API and relying on a third-party client for signal generation. Additionally, recognizing the diverse tool chains used in robotics and data science, we plan to develop a dedicated Python API client. This will broaden the framework's usability beyond MATLAB, allowing seamless integration with modern machine learning pipelines. Furthermore, we are exploring a porting of the framework to NVIDIA Isaac Sim and Cosys-AirSim, which would allow SonoTraceUE to serve as the acoustic sensing backend for a standardized, high-fidelity robotics simulation ecosystem. Beyond research, the visual nature of the Unreal Engine environment positions SonoTraceUE as a powerful educational tool. It allows students and researchers to visualize otherwise invisible acoustic phenomena, bridging the gap between theoretical acoustics and practical sensor behavior.

DECLARATION OF GENERATIVE AI USAGE

Generative AI was used in the creation of this article, specifically Microsoft's Copilot LLM, to improve the readability of some figures in this manuscript by generating MATLAB code to enhance their layout and style.

REFERENCES

- [1] J. Pacheco-Chérrez, J. A. Fortoul-Díaz, F. Cortés-Santacruz, L. María Alosó-Valerdi, and D. I. Ibarra-Zarate, "Bearing fault detection with vibration and acoustic signals: Comparison among different machine learning classification methods," *Engineering Failure Analysis*, vol. 139, p. 106515, 2022. [Online]. Available: <https://www.sciencedirect.com/science/article/pii/S1350630722004897>
- [2] A. Alousif and S. Alali, "Machinery Fault Detection Through Ultrasound Technology," in *SPE Middle East Oil & Gas Show and Conference*. OnePetro, Dec. 2021.
- [3] A. Dadouche, A. Rezaei, V. Wickramasinghe, W. Dmochowski, J. W. Bird, and F. Nitzsche, "Sensitivity of Air-Coupled Ultrasound and Eddy Current Sensors to Bearing Fault Detection," *Tribology Transactions*, vol. 51, no. 3, pp. 310–323, May 2008.
- [4] P. Kundu, "Review of rotating machinery elements condition monitoring using acoustic emission signal," *Expert Systems with Applications*, vol. 252, p. 124169, 2024. [Online]. Available: <https://www.sciencedirect.com/science/article/pii/S0957417424010352>
- [5] J. Steckel, A. Aerts, E. Verreycken, D. Laurijssen, and W. Daems, "Tool Wear Prediction in CNC Turning Operations using Ultrasonic Microphone Arrays and CNNs," Jun. 2024.
- [6] T. Guenther and A. Kroll, "Automated detection of compressed air leaks using a scanning ultrasonic sensor system," in *2016 IEEE Sensors Applications Symposium (SAS)*, Apr. 2016, pp. 1–6.
- [7] T. Wang, X. Wang, and M. Hong, "Gas leak location detection based on data fusion with time difference of arrival and energy decay using an ultrasonic sensor array," *Sensors*, vol. 18, no. 9, 2018. [Online]. Available: <https://www.mdpi.com/1424-8220/18/9/2985>
- [8] A. Schenck, W. Daems, and J. Steckel, "Toward automated air leak localization: A machine learning-enhanced ultrasonic and lidar-slam framework for industrial environments," *IEEE Access*, vol. 13, pp. 66 492–66 504, 2025.
- [9] J. Steckel and H. Peremans, "Biomimetic sonar for biomimetic SLAM," *Proceedings of IEEE Sensors*, pp. 2223–2226, 2012.
- [10] W. Jansen, D. Laurijssen, and J. Steckel, "Real-time sonar fusion for layered navigation controller," *Sensors*, vol. 22, no. 9, pp. 1–18, 2022.
- [11] A. Meliones, C. Filios, and J. Llorente, "Reliable ultrasonic obstacle recognition for outdoor blind navigation," *Technologies*, vol. 10, no. 3, 2022. [Online]. Available: <https://www.mdpi.com/2227-7080/10/3/54>

- [12] H.-U. Schnitzler, C. F. Moss, and A. Denzinger, "From spatial orientation to food acquisition in echolocating bats," *Trends in Ecology & Evolution*, vol. 18, no. 8, pp. 386–394, 2003.
- [13] I. Geipel, K. Jung, and E. K. Kalko, "Perception of silent and motionless prey on vegetation by echolocation in the gleaning bat *Micronycteris microtis*," *Proceedings of the Royal Society B: Biological Sciences*, vol. 280, no. 1754, p. 20122830, 2013.
- [14] M. G. Schöner, C. R. Schöner, R. Simon, T. U. Grafe, S. J. Puechmaille, L. L. Ji, and G. Kerth, "Bats are acoustically attracted to mutualistic carnivorous plants," *Current Biology*, vol. 25, no. 14, pp. 1911–1916, 2015.
- [15] X. Chen, C. Pan, J. Chen, and J. Benesty, "Planar array geometry optimization for region sound acquisition," in *ICASSP 2021 - 2021 IEEE International Conference on Acoustics, Speech and Signal Processing (ICASSP)*, 2021, pp. 756–760.
- [16] R. Umadi, "Widefield acoustics heuristic: advancing microphone array design for accurate spatial tracking of echolocating bats," *BMC Ecology and Evolution*, vol. 25, no. 1, p. 92, 2025.
- [17] Z. B. Rivera, M. C. De Simone, and D. Guida, "Unmanned ground vehicle modelling in gazebo/ros-based environments," *Machines*, vol. 7, no. 2, 2019. [Online]. Available: <https://www.mdpi.com/2075-1702/7/2/42>
- [18] D. Schröder and M. Vorländer, "Raven: A real-time framework for the auralization of interactive virtual environments," in *Forum acusticum*, vol. 27. Aalborg Denmark, 2011.
- [19] A. Anonymous, "EchoPT: A Pretrained Transformer Architecture for Predicting 2D In-Air Sonar Images in Mobile Robotics," May 2024.
- [20] M. Alves, F. Peixoto, A. Costa, and M. J. Nicolau, "Parking state monitoring via ultrasonic sensors: Large scale co-simulation validation," in *2025 Sixteenth International Conference on Ubiquitous and Future Networks (ICUFN)*, 2025, pp. 139–144.
- [21] C. Chen, J. Ramos, A. Tomar, and K. Grauman, "Sim2real transfer for audio-visual navigation with frequency-adaptive acoustic field prediction," in *2024 IEEE/RSJ International Conference on Intelligent Robots and Systems (IROS)*, 2024, pp. 8595–8602.
- [22] R. Simon, S. Rupitsch, M. Baumann, H. Wu, H. Peremans, and J. Steckel, "Bioinspired sonar reflectors as guiding beacons for autonomous navigation," *Proceedings of the National Academy of Sciences of the United States of America*, vol. 117, no. 3, pp. 1367–1374, 2020.
- [23] H. Zhu, A. K. Gupta, X. Wu, M. Goldsworthy, R. Wang, M. Mikkilineni, and R. Müller, "A validation study for a bat-inspired sonar sensing simulator," *PLOS ONE*, vol. 18, no. 1, p. e0280631, Jan. 2023.
- [24] M. H. Tanveer, X. Wu, A. Thomas, C. Ming, R. Müller, P. Tokekar, and H. Zhu, "A simulation framework for bio-inspired sonar sensing with unmanned aerial vehicles," *PLOS ONE*, vol. 15, no. 11, pp. 1–17, 11 2020. [Online]. Available: <https://doi.org/10.1371/journal.pone.0241443>
- [25] A. D. Pierce, *Acoustics: An Introduction to Its Physical Principles and Applications*. Springer, 2019.
- [26] W. Jansen and J. Steckel, "Sonotracelab—a raytracing-based acoustic modeling system for simulating echolocation behavior of bats," *IEEE Access*, vol. 12, pp. 69 371–69 382, 2024.
- [27] Epic Games, "Unreal engine." [Online]. Available: <https://www.unrealengine.com>
- [28] Youtube, Cosys-Lab, "Hardware-accelerated geometrical simulation of biological and engineered in-air ultrasonic systems," https://www.youtube.com/watch?v=_Z39IImT22E, 2026.
- [29] F. Ihlenburg, *Finite Element Analysis of Acoustic Scattering*. Springer, 1998.
- [30] L. L. Thompson, "A review of finite-element methods for time-harmonic acoustics," *The Journal of the Acoustical Society of America*, vol. 119, no. 3, pp. 1315–1330, 2006.
- [31] S. Kirkup, "The boundary element method in acoustics: A survey," *Applied Sciences*, vol. 9, no. 8, p. 1642, 2019.
- [32] C. COMSOL, "COMSOL: Multiphysics Software for Optimizing Designs," <https://www.comsol.com/>.
- [33] Ansys, "Ansys acoustics analysis," <https://www.ansys.com/products/acoustics>
- [34] NX Siemens, "Siemens NX Acoustics," <https://plm.sw.siemens.com/en-US/simcenter/simulation-test/acoustic-simulation/>.
- [35] B. E. Treeby and B. T. Cox, "K-Wave: MATLAB toolbox for the simulation and reconstruction of photoacoustic wave fields," *Journal of biomedical optics*, vol. 15, no. 2, pp. 021 314–021 314–12, 2010.
- [36] F.-I. Field-II, "Field II Ultrasound Simulation Program," <https://field-ii.dk/>.
- [37] X. Cao, Y. Cai, and X. Cui, "A parallel numerical acoustic simulation on a GPU using an edge-based smoothed finite element method," *Advances in Engineering Software*, vol. 148, p. 102835, 2020.
- [38] J. B. Allen and D. A. Berkley, "Image method for efficiently simulating small-room acoustics," *The Journal of the Acoustical Society of America*, vol. 65, no. 4, pp. 943–950, 04 1979. [Online]. Available: <https://doi.org/10.1121/1.382599>
- [39] K. Onaka, M. Morise, and T. Nishiura, "A design of 3-dimensional sound field simulator based on acoustic ray tracing and HRTF," in *2009 IEEE 13th International Symposium on Consumer Electronics*. IEEE, 2009, pp. 233–236.
- [40] N. Röber, S. Andres, and M. Masuch, *HRTF Simulations through Acoustic Raytracing*. Universitäts-und Landesbibliothek Sachsen-Anhalt, 2006.
- [41] N. Röber, U. Kaminski, and M. Masuch, "Ray acoustics using computer graphics technology," in *10th International Conference on Digital Audio Effects (DAFx-07)*, S, 2007, pp. 117–124.
- [42] Odeon A/S, "Odeon room acoustic software acoustics analysis," <https://odeon.dk/>.
- [43] AFMG Technologies GmbH, "Ease," <https://www.afmg.eu/en/ease>.
- [44] Siemens, "Siemens Ray Acoustics Modeling," <https://blogs.sw.siemens.com/simcenter/ray-acoustics-modeling/>.
- [45] T. M. Inc., "Audio toolbox," Natick, Massachusetts, United States, 2026. [Online]. Available: <https://www.mathworks.com>
- [46] J. Breton and G. Zanchelli, "(computational room acoustic module (cram))," 2021. [Online]. Available: <https://github.com/gregzanch/cram>
- [47] S. Liu and D. Manocha, "Sound synthesis, propagation, and rendering: A survey," 2021. [Online]. Available: <https://arxiv.org/abs/2011.05538>
- [48] C. Cao, Z. Ren, C. Schissler, D. Manocha, and K. Zhou, "Interactive sound propagation with bidirectional path tracing," *ACM Trans. Graph.*, vol. 35, no. 6, Dec. 2016. [Online]. Available: <https://doi.org/10.1145/2980179.2982431>
- [49] C. Schissler, R. Mehra, and D. Manocha, "High-order diffraction and diffuse reflections for interactive sound propagation in large environments," *ACM Trans. Graph.*, vol. 33, no. 4, Jul. 2014. [Online]. Available: <https://doi.org/10.1145/2601097.2601216>
- [50] U. Finnendahl, M. Worchel, T. Jüterbock, D. Wujecki, F. Brinkmann, S. Weinzierl, and M. Alexa, "Differentiable geometric acoustic path tracing using time-resolved path replay backpropagation," *ACM Trans. Graph.*, vol. 44, no. 4, Jul. 2025. [Online]. Available: <https://doi.org/10.1145/3730900>
- [51] N. Koenig and A. Howard, "Design and use paradigms for Gazebo, an open-source multi-robot simulator," *2004 IEEE/RSJ International Conference on Intelligent Robots and Systems (IROS)*, vol. 3, pp. 2149–2154, 2004.
- [52] NVIDIA, "Isaac Sim." [Online]. Available: <https://github.com/isaac-sim/IsaacSim>
- [53] A. Dosovitskiy, G. Ros, F. Codevilla, A. López, and V. Koltun, "CARLA: An Open Urban Driving Simulator," in *Proceedings of the 1st Annual Conference on Robot Learning*, 2017, pp. 1–16.
- [54] W. Jansen, E. Verreycken, A. Schenck, J.-E. Blanquart, C. Verhulst, N. Huebel, and J. Steckel, "Cosys-airsim: A real-time simulation framework expanded for complex industrial applications," in *2023 Annual Modeling and Simulation Conference (ANNSIM)*, 2023, pp. 37–48.
- [55] A. Schenck, W. Jansen, W. Daems, and J. Steckel, "Airleaksim: Using cosys-airsim to benchmark different pressurized airleak localization strategies," *IEEE Sensors Journal*, vol. 26, no. 1, pp. 826–835, 2026.
- [56] M. Meyer, M. Desbrun, P. Schröder, and A. H. Barr, "Discrete differential-geometry operators for triangulated 2-manifolds," in *Visualization and Mathematics III*, H.-C. Hege and K. Polthier, Eds. Berlin, Heidelberg: Springer Berlin Heidelberg, 2003, pp. 35–57.
- [57] P. Leopardi, "A partition of the unit sphere into regions of equal area and small diameter," *Electronic Transactions on Numerical Analysis*, vol. 25, no. 12, pp. 309–327, 2006.
- [58] M. Corsini, P. Cignoni, and R. Scopigno, "Efficient and flexible sampling with blue noise properties of triangular meshes," *IEEE transactions on visualization and computer graphics*, vol. 18, no. 6, pp. 914–924, 2012.
- [59] J. Steckel and H. Peremans, "A novel biomimetic sonarhead using beamforming technology to mimic bat echolocation," *IEEE transactions on ultrasonics, ferroelectrics and frequency control*, vol. 59, no. 7, pp. 1369–1377, 2012.
- [60] E. Verreycken, R. Simon, B. Quirk-Royal, W. Daems, J. Barber, and J. Steckel, "Bio-acoustic tracking and localization using heterogeneous, scalable microphone arrays," *Communications Biology*, vol. 4, no. 1, p. 11 p., 2021.
- [61] E. L. Clare and M. W. Holderied, "Acoustic shadows help gleanings bats find prey, but may be defeated by prey acoustic camouflage on rough surfaces," *eLife*, vol. 4, p. e07404, Sep. 2015.
- [62] R. Stabler, "Beach pebbles 3d model," <https://skfb.ly/6p6OR>, 2017.

- [63] D. Laurijssen, W. Jansen, A. Aerts, W. Daems, and J. Steckel, "Ruggedized embedded ultrasound sensing in harsh conditions: ertis in the wild," pp. 975–985, 2026.
- [64] J. Steckel, A. Boen, and H. Peremans, "Broadband 3-d sonar system using a sparse array for indoor navigation," *IEEE Transactions on Robotics*, vol. 29, no. 1, pp. 161–171, 2013.
- [65] J. Steckel and H. Peremans, "BatSLAM : Simultaneous localization and mapping using biomimetic sonar," *PLoS ONE*, vol. 8, no. 1, pp. 1–11, 2013.
- [66] —, "Spatial sampling strategy for a 3d sonar sensor supporting batslam," in *2015 IEEE/RSJ International Conference on Intelligent Robots and Systems (IROS)*, Sep. 2015, pp. 723–728.
- [67] Y. Pan, X. Zhong, L. Wiesmann, T. Posewsky, J. Behley, and C. Stachniss, "Pin-slam: Lidar slam using a point-based implicit neural representation for achieving global map consistency," *IEEE Transactions on Robotics*, vol. 40, pp. 4045–4064, 2024.
- [68] Github, Cosys-Lab, "SonoTraceUE Source Repository," <https://github.com/Cosys-Lab/SonoTraceUE>, 2026.
- [69] Mathworks MATLAB File Exchange, Cosys-Lab, "SonoTraceUE Matlab Toolbox," <https://www.mathworks.com/matlabcentral/fileexchange/183020-sonotraceue-matlab-toolbox>, 2026.